Eur. Phys. J. Plus (2024) 139:34
https://doi.org/10.1140/epjp/s13360-023-04821-5

THE EUROPEAN PHYSICAL JOURNAL PLUS

Regular Article

Magnetic behavior of a diatomic molecule with spin-1 on the Bethe lattice

Erhan Albayrak[a]

Department of Physics, Erciyes University, 38039 Kayseri, Turkey

Received: 11 November 2023 / Accepted: 22 December 2023
© The Author(s) 2024

Abstract Thermal fluctuations in magnetizations and magnetic phase diagrams of a diatomic molecule are investigated on the Bethe lattice (BL) with coordination number $q = 3$ by using the exact recursion relations (ERR). Each molecule is assumed to interact with others via its atoms in terms of various bilinear interaction parameters. They involve the interaction of atoms within each molecule as well as the interaction of atoms between the molecules. Each site is also considered to have an active crystal field. Following the determination of the average magnetization of the molecule and its atoms in the central molecule of the BL in terms of ERR, their thermal fluctuations and potential phase diagrams are thoroughly analyzed. Numerous phase regions, ordered (O), i.e., ferromagnetic (FM) or antiferromagnetic (AFM), paramagnetic (P), and random (R), are discovered. The phase boundaries between these phases are obtained in terms of first- and second-order and random phase transition lines. Therefore, various critical phenomena, including tricritical point (TCP), bicritical point (BCP), critical end point (CEP) and reentrant behavior (RB), are observed.

1 Introduction

After the discovery of the Ising model consisting of spin-1/2 atoms with a bilinear interaction parameter (J) between the nearest-neighbor (NN) spins [1], the Blume-Capel (BC) model with spin-1 was obtained, presenting the first- and second-order phase lines with a TCP and so on to higher spin models [2, 3]. Then, many variations of these models were carried out, such as mixed-spin models, higher neighbor interactions, and various types of geometrical structures, each presenting new types of critical phenomena, including compensation temperatures, frustrations, etc. These works were not only considered on real lattices but also on some recursive ones.

Several theoretical studies on recursive lattices, including those by Kagome, Husimi, Bethe, and others, have revealed frustrations in magnetization or other thermodynamic functions when different forms of bilinear exchange interactions or some other system parameters are varied. Some of them for spin-1 may be listed as follows: The three-dimensional (3D) axial next NN Ising model was studied by considering the FM intra- and inter-layer interactions and two types of competing AFM interactions between next-nearest layers [4]. The magnetization plateau at 1/4 of the saturation magnetization of the AFM spin ladder was obtained [5]. The quantum phase transitions in a quasi-1D orthogonal-dimer spin chain were investigated by means of exact diagonalization, taking into account the effect of the interchain coupling [6]. The magnetization process of an Ising-type spin chain with NN interaction (J_1), next NN interaction (J_2), and single-ion anisotropy (D) was investigated on the basis of the ground state phase diagram in a magnetic field [7]. The XXZ model with next NN interaction and Ising-type anisotropy was studied by using a numerical diagonalization technique [8]. An exactly solvable system in which frustration is present due to competing biquadratic and crystal-field interactions was presented [9]. The Kagome antiferromagnets with an isotropic Heisenberg exchange J and strong easy-axis single-ion anisotropy D were studied [10] and reviewed in the low-temperature phases, in which there is a sufficiently strong D that dominates over the AFM exchange J [11]. The ground-state properties of AFM NN interactions on a triangular lattice were investigated in the presence of an external magnetic field [12]. 2D frustrated Heisenberg antiferromagnets with single-ion anisotropy on a square lattice at low temperatures [13] and with both spin and spatial anisotropies and the competitive next NN interaction at zero temperature [14] were investigated using spin-wave theory. The second-order phase transitions of the FM Ising model on pure Husimi lattices built up from elementary triangles [15, 16] and elementary squares [17] were studied, and a similar study on tetrahedron recursive lattices was also carried out [18]. The magnetic and thermodynamic properties of anisotropic frustrated Heisenberg antiferromagnet on a body-centered cubic lattice were investigated by the use of double-time Green's function within the random phase approximation together with Anderson and Callen's decoupling [19]. A comprehensive investigation of the crystal structure and magnetic behavior of the compound $Ba_2Ni(PO_4)_2$ with a honeycomblike topology of the spin–lattice was reported [20]. The magnetic behavior of a single-walled hexagonal Ising nanotube was investigated using the effective field theory with correlations and the differential operator technique [21]. The ground-state (GS) phases of alternating-bond diamond chains were examined [22]. The GS phase

[a] e-mail: albayrak@erciyes.edu.tr (corresponding author)

Published online: 08 January 2024

diagrams and magnetization curves of a Heisenberg diamond cluster with two different coupling constants and uniaxial single-ion anisotropy were investigated in the presence of external magnetic field by using exact diagonalization techniques [23]. The NN AFM Heisenberg model considered for spins with spin-1/2 and spin-1 located on the vertices of a dodecahedron and icosahedron [24]. The spontaneously magnetized Tomonaga-Luttinger liquid was studied in geometrically frustrated quasi-1D quantum magnets on a union-jack lattice [25]. The $J_1 - J_2$ Heisenberg model with first and second neighbor AFM exchange interactions was considered by using the modified spin wave method [26] and a classical MC analysis [27]. Isotropic Heisenberg model on a trellis ladder which is composed of two $J_1 - J_2$ zigzag ladders interacting through AFM rung coupling J_3 was analyzed [28]. The effect of four-spin cyclic exchange interaction at each plaquette in two-leg spin ladder was investigated at $T = 0$, focusing especially on the field-induced gap [29]. The MC simulation was used to study the magnetic properties of Ising AFM film sandwiches between two ferromagnetic surfaces with different exchange surface interactions [30]. The thermodynamic properties of an Ising cluster with a centered tetrakis hexahedron structure were studied by employing exact enumeration [31]. Using the density-matrix renormalization group technique, 1D Heisenberg chain consisting of coupled tetramers was examined as an effective spin model for the copper vanadate CuInVO5 [32]. 1D Heisenberg model with AFM NN J_1 and next NN J_2 exchange couplings in magnetic field h was studied [33]. The zero-temperature phase diagram of the $J_1 - J_2 - J_3 - J_1^{\perp}$ model on an AA-stacked square-lattice bilayer was studied using the coupled cluster method implemented to very high orders [34] and for the case with frustration [35].

The experimental evidence for the existence of frustrations in various spin-1 models were also reported. The 1/4 plateau in high-field magnetization measurement on the organic spin ladder compound BIP-TENO was presented, and the theoretical mechanism of the plateau formation was proposed based on the frustrated interactions [36] and third-neighbor exchange interactions [37]. Magnetization and bulk susceptibility of Haldane chain system doped with electronic holes have been measured and found that the existence of FM bonds induce magnetic frustration when interchain interactions come into play at low temperatures [38]. The GS of organic Heisenberg AFM m-MPYNN.BF4, a 2D Kagome lattice of dimers with a small trigonal distortion, was investigated by measuring the AC susceptibility and the magnetization as a function of the magnetic field [39]. A nonclassical magnetization plateau at one-third of the saturation magnetization that was driven by spin frustration and quantum fluctuations was reported for the magnetization and specific heat measurements on $Ba_3NiSb_2O_9$ which is a quasi-2D triangular-lattice antiferromagnet [40]. The ferromagnetism and spin-glass-like behavior in polycrystalline perovskite based on the investigations of magnetization, magnetic AC susceptibility, and electron spin resonance revealed that the spin-glass phenomenon related to the magnetic frustration was caused by the strong competition between FM and AFM interactions [41]. The crystal structure and preliminary magnetization measurements on the Kagome antiferromagnet, $NH_4Ni_{2.5}V_2O_7(OH)_2{\cdot}H_2O$, presented clear evidence of frustration and competition between FM and AFM interactions [42]. Thermal entanglement of the spin-1 Ising-Heisenberg diamond chain was considered for the isotropic Heisenberg (Ising-XXX) and anisotropic Heisenberg (Ising-XXZ) coupling models [43]. The magnetic phase diagram of piezomagnetic Mn_3NiN thin films, a frustrated noncollinear AFM structure, was studied as a function of the growth-induced biaxial strain [44]. The critical properties of the honeycomb AFM $BaNi_2V_2O_8$ both below and above the Néel temperature were determined using neutron diffraction and muon spin rotation measurements [45]. A detailed lattice structure, magnetization and specific heat measurements on the triple-perovskite material $Sr_3CuIr_2O_9$ were reported [46]. The crystal structure and magnetic properties of $Y_3Cu_9(OH)_{19}Cl_8$ were determined from single crystal X-ray diffraction and confirmed by neutron powder diffraction [47].

As seen from the above works, the tailoring of spin models continues to give vast variety of critical phenomena. It is also clear that they are mostly carried out for the GS's with zero temperature, NN and next NN models or with the addition of external magnetic field which reduces the number of freedom for a given system. It should also be mentioned that the existing BL studies assume that each site is occupied by a single particle, see for example [48–50]. Those single particles are actually made up by the addition of subparticles. To investigate the further details of the model, it may be better to study behavior of each particle by considering its subparticles. The starting point may be the study of diatomic molecules on the BL then it can be extended to molecules with higher numbers of atoms.

Therefore, in this work, we assume that diatomic molecules, in which each atom is spin-1, occupy the BL sites instead of single particles. Then, each NN molecule is allowed to interact via their atoms A and B with six different possible J's. Each site is also assumed to be under the effect of crystal field D. After obtaining the formulation in terms of ERRs, the numerical analysis of the model is simplified by reducing the number of J's to three because of the symmetry. Then, the phase diagrams are obtained on the (D, T) planes by studying the thermal variations of the central diatomic molecule and its atoms for the coordination number of $q = 3$ when $J < 0$ and $J > 0$ cases correspond to AFM and FM phases, respectively. As it will be clear later in the work, very interesting new critical phenomena and phase diagrams were obtained.

The rest of this work is structured as follows: The following part formulates the problem on the BL in terms of molecule constituents. The third section is set aside to investigate the thermal fluctuations of the molecules and their constituents, as well as the potential phase diagrams. The final section contains a summary and conclusions.

2 The formulation

The assumed Hamiltonian of the diatomic molecules in terms of the bilinear interaction parameters (J) between the atoms of a molecule and between the atoms of NN molecules and the crystal field (D) may be presented as

$$\begin{aligned}\mathcal{H} = &- \sum_{<i,i>} J_{A^iB^i}\sigma_A^i\sigma_B^i - \sum_{<i,i+1>} J_{A^iA^{i+1}}\sigma_A^i\sigma_A^{i+1} \\ &- \sum_{<i,i+1>} J_{B^iB^{i+1}}\sigma_B^i\sigma_B^{i+1} - \sum_{<i,i+1>} J_{A^iB^{i+1}}\sigma_A^i\sigma_B^{i+1} \\ &- \sum_{<i,i+1>} J_{B^iA^{i+1}}\sigma_B^i\sigma_A^{i+1} - D\sum_i (\sigma_A^i)^2 - D\sum_i (\sigma_B^i)^2 \end{aligned} \tag{1}$$

where A and B indicate the atoms that may be taken to be the same type or not, and i counts the number of shells on the BL, i.e., the central shell is the central molecule starting with $i = 0$ and $i \to \infty$ in the thermodynamic limit as shown in Fig. 1. It should be noted that this type of Hamiltonian with different J values between the constituents of molecules allows the design of various theoretical spin models according to the spin summation rules.

In this study, the same procedure on the BL as obtained for the single-spin systems [51] is followed. The BL is set up in such a way that the central molecule, $i = 0$, has two spin-1, σ_A^0 and σ_B^0 interacting via $J_{A^0B^0}$, to which q NN molecules of the same type, i.e., the first shell molecules, are connected. Then, each molecule of the first shell is connected with $q-1$ molecules. This procedure is applied until the thermodynamic limit is reached, which occurs when the number of shells go to infinity.

In working with the ERR approach, one starts with the partition function defined as

$$Z = \sum e^{-\beta\hat{\mathcal{H}}} = \sum_{Spc} P(Spc) \tag{2}$$

where P_{Spc} is usually thought of as an unnormalized probability distribution over the spin-configurations (Spc) and $\beta = 1/kT$ is the inverse temperature. It can be written for the central molecule as

$$P(\sigma_A^0, \sigma_B^0) = e^{\beta[J_{A^0B^0}(\sigma_A^0\sigma_B^0) + D(\sigma_A^0)^2 + D(\sigma_B^0)^2]} \prod_{j=1}^{q} Q_n(\{\sigma_A^0, \sigma_B^0\}|\{\sigma_A^1, \sigma_B^1\}^j) \tag{3}$$

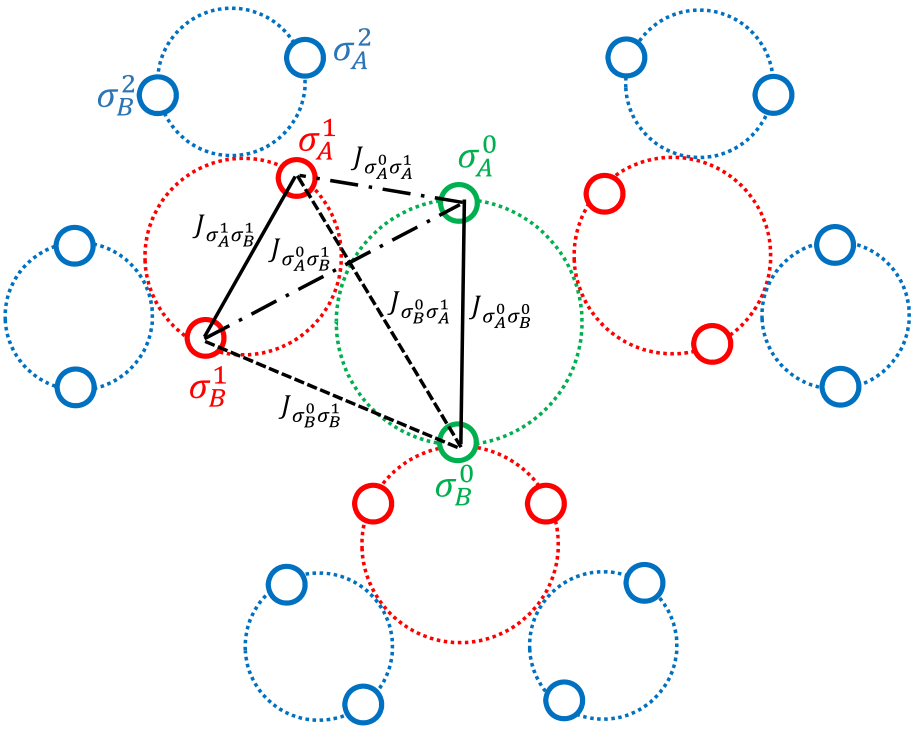


Fig. 1 The schematic representation of the BL in terms of the molecules and their atoms. Each molecule has two atoms of A and B with spin-1 and $q = 3$. Big dashed circles represent molecules, while small solid circles indicates their atoms. Bilinear interaction parameters inside each molecule are denoted with $J_{\sigma_A^i\sigma_B^i}$. In addition, the NN molecules interact via their atoms with $J_{\sigma_A^i\sigma_A^j}$, $J_{\sigma_A^i\sigma_B^j}$ and $J_{\sigma_B^i\sigma_B^j}$

where

$$Q_n(\{\sigma_A^0,\sigma_B^0\}|\{\sigma_A^1,\sigma_B^1\}) = e^{\beta[J_{A^1B^1}(\sigma_A^1\sigma_B^1)+D(\sigma_A^1)^2+D(\sigma_B^1)^2]} \times e^{\beta J_{A^1A^0}(\sigma_A^1\sigma_A^0)} \times e^{\beta J_{A^1B^0}(\sigma_A^1\sigma_B^0)} \times e^{\beta J_{B^1A^0}(\sigma_B^1\sigma_A^0)} \times e^{\beta J_{B^1B^0}(\sigma_B^1\sigma_B^0)} \times \quad e^{\texttt{All other interactions for given branches of BL}}. \tag{4}$$

It is obtained by cutting the BL at the first shell containing q molecules and each of which has $q-1$ NN from the second shell. Thus, it is given as

$$Q_n(\{\sigma_A^0,\sigma_B^0\}|\{\sigma_A^1,\sigma_B^1\}) = e^{\beta[J_{A^1B^1}(\sigma_A^1\sigma_B^1)+D(\sigma_A^1)^2+D(\sigma_B^1)^2]} \times e^{\beta J_{A^1A^0}(\sigma_A^1\sigma_A^0)} \times e^{\beta J_{A^1B^0}(\sigma_A^1\sigma_B^0)} \times e^{\beta J_{B^1A^0}(\sigma_B^1\sigma_A^0)} \times e^{\beta J_{B^1B^0}(\sigma_B^1\sigma_B^0)} \times \prod_{j=1}^{q-1} Q_{n-1}(\{\sigma_A^1,\sigma_B^1\}|\{\sigma_A^2,\sigma_B^2\}^j). \tag{5}$$

This procedure is followed until the thermodynamic limit, but for our purposes, the consideration of the first two shells is enough because of the symmetry. The thermodynamic limit is then reached by simple iterations.

Now, one can get a function giving the weight of each possible spin configurations defined for the central molecule as

$$g_n(\{\sigma_A^0,\sigma_B^0\}) = \sum_{\{\sigma_A^1,\sigma_B^1\}} Q_n(\{\sigma_A^0,\sigma_B^0\}|\{\sigma_A^1,\sigma_B^1\}) \tag{6}$$

which is calculated for given spin values of ±1 and 0 for $\{\sigma_A^0,\ \sigma_B^0\}$ by summing over the spin values of ±1 and 0 for $\{\sigma_A^1,\ \sigma_B^1\}$. Since each molecule has two spins of spin-1 with three possible values, one gets nine ground state configurations and thus nine g_n values. As a result, eight ERRs can be obtained by dividing the g_n functions, with any one of them, which is chosen $g_n(0,\ 0)$. Thus, they are given as

$$X_1 = \frac{g_n(1,1)}{g_n(0,0)}, X_2 = \frac{g_n(1,0)}{g_n(0,0)}, X_3 = \frac{g_n(1,\ -1)}{g_n(0,0)}, X_4 = \frac{g_n(-1,1)}{g_n(0,0)},$$
$$X_5 = \frac{g_n(-1,0)}{g_n(0,0)}, X_6 = \frac{g_n(-1,\ -1)}{g_n(0,0)}, X_7 = \frac{g_n(0,1)}{g_n(0,0)}, X_8 = \frac{g_n(0,\ -1)}{g_n(0,0)} \tag{7}$$

which are presented explicitly in the Appendix.

Now, we are ready to obtain the partition function, thus, the magnetizations of constituents of the core molecule. The partition function is defined in terms of g_n functions by using Eqs.(2) and (3) as

$$Z = \sum_{\{\sigma_A^0,\sigma_B^0\}} P(\sigma_A^0,\sigma_B^0) = \sum_{\{\sigma_A^0,\sigma_B^0\}} e^{\beta[J_{A^0B^0}(\sigma_A^0\sigma_B^0)+D(\sigma_A^0)^2+D(\sigma_B^0)^2]}[g_n(\sigma_A^0,\sigma_B^0)]^q, \tag{8}$$

and found for the given values of $\sigma_A^0,\ \sigma_B^0 = \pm1,\ 0$ as

$$Z = e^{\beta(2D+J_{A^0B^0})}[g_n(1,1)]^q + e^{\beta D}[g_n(1,0)]^q + e^{\beta(2D-J_{A^0B^0})}[g_n(1,\ -1)]^q + e^{\beta(2D-J_{A^0B^0})}[g_n(-1,1)]^q + e^{\beta D}[g_n(-1,0)]^q + e^{\beta(2D+J_{A^0B^0})}[g_n(-1,\ -1)]^q + e^{\beta D}[g_n(0,1)]^q + e^{\beta D}[g_n(0,\ -1)]^q + [g_n(0,0)]^q \tag{9}$$

The magnetizations of the atoms of central molecule is defined as

$$M_\alpha = \frac{1}{Z}\sum_{\{\sigma_A^0,\sigma_B^0\}} \sigma_\alpha^0 e^{\beta[J_{A^0B^0}(\sigma_A^0\sigma_B^0)+D(\sigma_A^0)^2+D(\sigma_B^0)^2]} \times [g_n(\sigma_A^0,\sigma_B^0)]^q, \quad \texttt{with} \ \ \alpha = A \ \texttt{or} \ B. \tag{10}$$

The magnetization of the A type atom of the core spin is calculated as

$$M_A = \frac{1}{Z_R}[e^{\beta(2D+J_{A^0B^0})}X_1^q + e^{\beta D}X_2^q + e^{\beta(2D-J_{A^0B^0})}X_3^q - e^{\beta(2D-J_{A^0B^0})}X_4^q - e^{\beta D}X_5^q - e^{\beta(2D+J_{A^0B^0})}X_6^q] \tag{11}$$

and for the B type atom of the core spin is given as

$$M_B = \frac{1}{Z_R}[e^{\beta(2D+J_{A^0B^0})}X_1^q - e^{\beta(2D-J_{A^0B^0})}X_3^q + e^{\beta(2D-J_{A^0B^0})}X_4^q - e^{\beta(2D+J_{A^0B^0})}X_6^q + e^{\beta D}X_7^q - e^{\beta D}X_8^q]. \tag{12}$$

with

$$Z_R = e^{\beta(2D+J_{A^0B^0})}X_1^q + e^{\beta D}X_2^q + e^{\beta(2D-J_{A^0B^0})}X_3^q + e^{\beta(2D-J_{A^0B^0})}X_4^q + e^{\beta D}X_5^q + e^{\beta(2D+J_{A^0B^0})}X_6^q + e^{\beta D}X_7^q + e^{\beta D}X_8^q + 1.0. \tag{13}$$

The net average magnetization of the central diatomic molecule is now defined as

$$M_N = \frac{1}{2}(M_A + M_B). \tag{14}$$

After having obtained all the formulation of the model in terms of the ERRs, we are now ready to calculate its variations for given values of J's and D's under temperature change to obtain the possible phase diagrams of the model.

3 The results and conclusions

One method for obtaining probable phase regions, phase transitions, and critical phenomena is to investigate temperature fluctuations in magnetizations. Because each BL site is encompassed by a diatomic molecule, the various ground states (GS) are determined by its atoms. Because each atom has a spin-1 with the values of ±1, 0, each molecule can have the GS values of ±2, ±1, 0. According to Eq.(13), the GS's of net average magnetization can be ±1, ±0.5, 0. This is based on the ordered phases being FM or AFM. Higher thermal agitations take the system to the P phase, for which magnetization becomes zero and appears after the critical temperatures. Since we have reduced the number of J's into three, because of the symmetry, and the active crystal field D at each site, their competition with each other and temperature leads to another phase in which magnetizations move up and down randomly, i.e., the R phase with zero or nonzero net magnetization, which is observed at low or high temperatures and at any values of D, like the ordered phases. It should be noted that we do not identify the different characteristics of the ordered phases depending on the spin configuration and just call them the ordered phase (O) for simplicity.

It should also be mentioned that the FM and AFM phases correspond to $J > 0$ and $J < 0$, respectively. In addition, we consider the case with $J_{A^iB^i} = J_{A^{i+1}B^{i+1}} = \pm1$, $J_{B^iA^{i+1}} = J_{A^iB^{i+1}} \pm 1$ and $J_{A^iA^{i+1}} = J_{B^iB^{i+1}} \pm 1$ for all $i = 1, 2, ..., N$ because of the symmetry. N goes to infinity in the thermodynamic limit. Therefore, we consider the configurations shown in Table 1 in accordance with Fig. 1.

Now, we present the thermal variations of magnetizations, M_A, M_B and M_N, according to Table 1.

3.1 Thermal fluctuations of magnetizations

The behaviors of M_N, M_A and M_B are demonstrated under the variations of D and T for $q = 3$ corresponding to the honeycomb lattice according to Table 1. M_N, M_A and M_B are shown with solid, dashed and dotted-dashed lines, respectively. The configurations are indicated with [...] in the figures.

Figure 2a, obtained for $D = 1.0$, presents the thermal changes of magnetizations for configuration A. As seen, M_N, M_A, and M_B start from 1.0, i.e., the GS. As T increases, they decrease and present jumps at the T_t, indicating first-order phase transition (FOPT), to the negative values, and then with the further increase of T, they go to zero continuously at the T_c, corresponding to

Table 1 Some configurations of the model for given $J = 1$ and $J = -1$ corresponding to FM and AFM phases, respectively. i and $j = i + 1$ represent the atoms of the central and NN molecules, and so on to other generations

Configuration	$J_{A^iB^i} = J_{A^jB^j}$	$J_{A^iB^j} = J_{B^iA^j}$	$J_{A^iA^j} = J_{B^iB^j}$
[A]	1	1	1
[B]	1	1	−1
[C]	1	−1	1
[D]	−1	1	1
[E]	1	−1	−1
[F]	−1	1	−1
[G]	−1	−1	1
[H]	−1	−1	−1

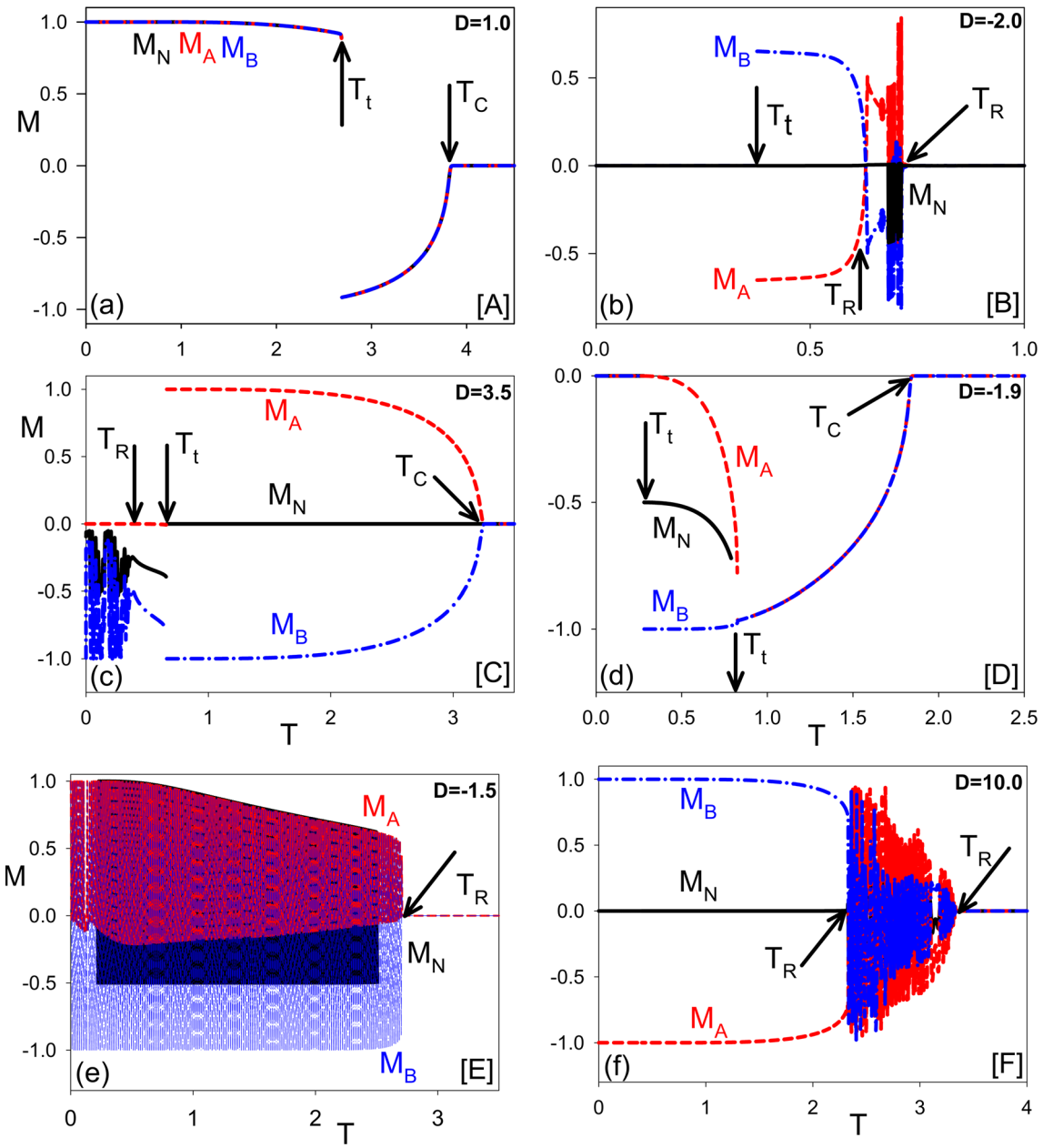


Fig. 2 Thermal variations of magnetizations indicated with black, red and blue lines for M_N, M_A and M_B and obtained for **a** $D = 1.0$ for [A], **b** $D = -2.0$ for [B], **c** $D = 3.5$ for [C], **d** $D = -1.9$ for [D], **e** $D = -1.5$ for [E] and **f** $D = 10.0$ for [F], respectively

second-order phase transition (SOPT). Configuration B is illustrated in Fig. 2b and shows that all magnetizations start from zero. Then, $M_A = -M_B$ appears at the T_t with $M_N = 0.0$ corresponding to the AFM phase. As soon as they disappear, the R phase starts at the first T_R and later it vanishes at the second T_R. The existence of two T_R's leads to reentrant behavior as will be seen later in the phase diagrams. Figure 2c for configuration C displays the R phase at zero temperature, which terminates at T_R with the start of the O phase. During which magnetizations present jumps with $M_A = -M_B$ appearing at the T_t and $M_N = 0.0$. With the further increase of T, $M_A = -M_B$ decreases continuously to zero at T_c. For configuration D, all magnetizations begin at zero, as shown in Fig. 2d. They begin with two jumps corresponding to two T_t's that lead to reentrant behavior. They all then vanish at T_c. It's worth noting that the model starts with the R phase and subsequently disappears at T_R with the start of the P phase, as seen in Fig. 2e for configuration E. The final illustration of this section is presented in Fig. 2f for the configuration F. We see that $M_A = -M_B$ appears at the T_t with $M_N = 0.0$ corresponding to the AFM phase again. The R phase starts at the first T_R and vanishes at the second T_R with the start of P phase.

It is clear from these figures that the model gives either a single phase, O or R, or multiple phases of O and R. They are separated from each other by the possible T_c-, T_t- or T_R-lines. Additionally, they may combine in different combinations, leading to various critical phenomena. They are now all presented in the phase diagrams.

3.2 The phase diagrams

As our final illustrations, we present the phase diagrams on the (D, T) planes according to the configurations given in Table 1. The T_c, T_t and T_R lines are shown by black solid, red dashed and blue dotted-dashed lines, respectively. O, R, and P represent the ordered, random, and paramagnetic phases, respectively. In addition, the model also displays some critical points such as the tricritical points (TCP) indicated with a solid circle, bicritical points (BCP) shown with a gray circle and critical end point (CEP) pointed out with an empty square.

It should be noted that the BC model gives T_c and T_t combined at the TCP [2, 3] which appears at negative D values. As D becomes more negative, it drives the model to the lowest spin value, that is zero for spin-1, leading to the appearance of T_t and thus TCP. Here, we also observe a similar behavior and additional new behaviors. The T_c, T_t and T_R lines are displayed for all values of D, in contrary to BC model which shows T_t for $D < 0.0$ only.

We are now ready to exhibit our phase diagrams, configuration by configuration, as seen in Table 1.

Configuration A (Fig. 3a): The T_c and T_t lines appear at higher T and D with $T_c > T_t$. The T_c line separates the O and P phases, while the T_t line separates two different types of O phases. This T_c line terminates at the TCP, indicated with a solid circle appearing at $D = -3.36$ and $T = 1.42$, from where a T_t line appears (as in the BC model) which terminates at $T = 0.0$ for $D \simeq -2.56$. Additionally, the first T_t line gradually decreases with decreasing D and then terminates on the second T_t line at the BCP indicated with an empty square found at $D = -3.15$ and $T = 0.8$.

Configuration B (Fig. 3b): In this case, the NN atoms of the same type interact antiferromagnetically, while the rest interact ferromagnetically. The phase lines are observed to be T_R lines, which enclose the R phase at higher D and T. As D decreases, they get closer to each other and then combine together, from where a T_t line emerges. This critical point is the BCP, indicated with a gray circle. With the further decrease of D, the T_t line terminates at the second BCP. Again, the T_R lines enclose the small R region and terminate at the third BCP. Then, the emergent T_t line terminates at zero temperature.

Configuration C (Fig. 3c): This figure is similar to Fig. 3a, but now we also see a random phase region observed at higher D and T separated from the O phase. The TCP at $D = -2.37$ and $T = 1.07$ and the CEP at $D = -2.22$ and $T = 0.65$ are lower since we have $J_{B^i A^{i+1}} = J_{A^i B^{i+1}} = -1.0$ which prefers AFM configuration, causing a decrease in magnetizations.

Configuration D (Fig. 3d): This figure is also similar to Fig. 3a and c, now one observes the TCP at $D = -2.37$ and $T = 1.12$ and the CEP at $D = -2.26$ and $T = 0.74$ are almost the same with Fig. 3b, since we have $J_{B^i A^i} = J_{A^i B^i} = -1.0$ which prefers the AFM phase inside molecule in contrast to configuration C which is for the AFM phase for NN molecules.

Configuration E (Fig. 3e): It is very interesting that the phase diagram consists of only two random phases, i.e., the P phase with $M = 0.0$ caused by thermal agitations and the R phase with $M \neq 0.0$ acquired by the frustrations. The T_R line also starts at higher T and D and as D decreases, its temperature decreases to terminate at zero T like the other critical lines of the model. Now, there is a small region of protrusion at low T and D displaying reentrant behavior because of the double T_R.

Configuration F (Fig. 3f): The phase diagram is qualitatively similar to Fig. 3b, now the R phase is observed at a higher T and encloses a larger region.

Configuration G (Fig. 3g): The qualitative similarity of this figure is clearly obvious compared to Figs. 3a, c and d. Now, the TCP is seen at $D = -3.35$ and $T = 1.49$ and the CEP is found at $D = -3.09$ and $T = 0.71$ which are very close to the values of Fig. 3a.

Configuration H (Fig. 3h): This phase diagram is analogous to Fig. 3e, appearing at lower T for higher D, with a shorter range in the $D < 0.0$ region, and with the protrusion being at a lower T than in Fig. 3e.

4 The summary and conclusions

Thermal variations of magnetizations for a diatomic molecule, which consists of spin-1 atoms A and B, placed at each site of a BL were studied in detail to obtain its critical behaviors. It is found that the competition between the three types of J's, chosen to be FM or AFM, D and T leads to very rich phase diagrams in comparison to the well-known BC model. First- and second-order, and random phase transition lines are observed, and their various combinations lead to various critical phenomena, including the TCP, BCP, CEP and RB.

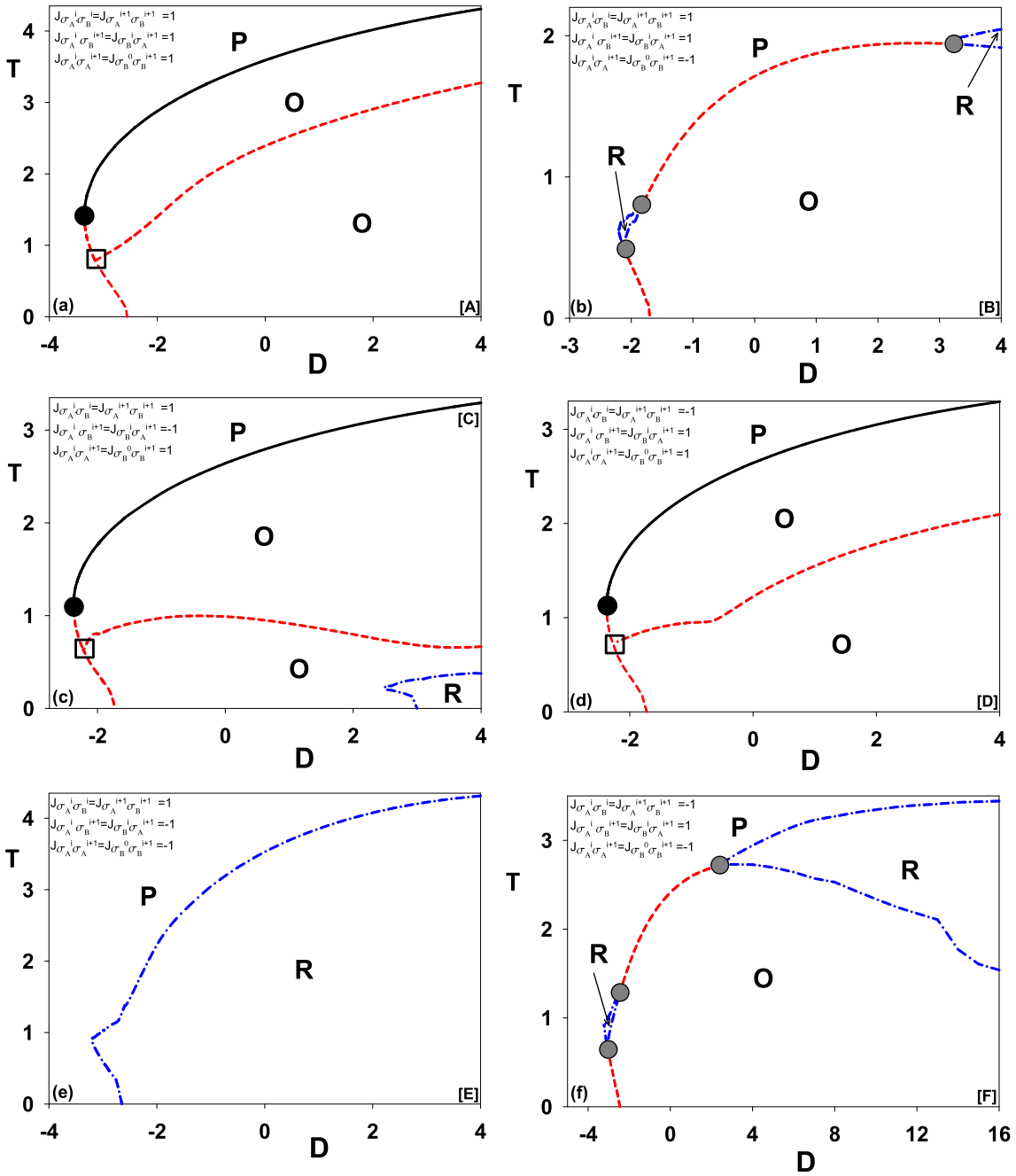


Fig. 3 The phase diagrams on the (T, D) planes for $J_{\sigma_A^i \sigma_B^i}$, $J_{\sigma_A^i \sigma_A^j}$, $J_{\sigma_A^i \sigma_B^j}$ and $J_{\sigma_B^i \sigma_B^j}$ according to Table 1 corresponding to the configurations [A]-[H], respectively. The T_c, T_t and T_R lines are indicated with black solid, red dashed and blue dotted-dashed lines

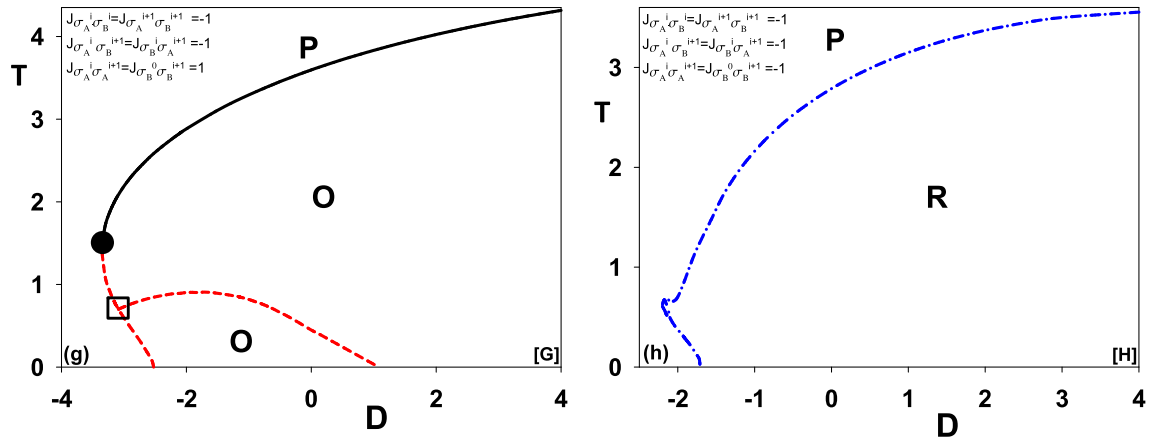


Fig. 3 continued

The formulation of the problem for diatomic molecules can easily be extended to higher molecules on the BL by using the ERR's which may serve to be advantageous over the other methods. This approach clearly brings out much more details for the system of single particles at each BL site which are clear from the presented phase diagrams. Our concluding remarks are as follows: (i) R phase is usually observed in between the O and P phases as in Fig. 3b and f, and also together with the P phase but at lower T and higher D values as in Fig. 3e and h, and separated from them by T_R lines, (ii) the TCP's are only observed between the T_c and T_t lines as in the BC model, (iii) the BCP's are only observed between the T_R and T_t lines, (iv) the CEP's are only found between the T_t lines, (v) RB is only exhibited as a protrusion in the T_R lines, (vi) R phase is usually observed before and after the AFM phase transitions that is when $M_A = -M_B$ as in Fig. 2b,c and f, (vii) R phase is also observed before the P phase, both of them are the disordered phases which is very interesting, as in Fig. 2e and (viii) as seen, Fig. 3a is very similar with the BC model phase diagram, but as the signs of J's changed to negative -1.0, the phase diagrams becomes more complex and new features come out. Note also that as D becomes more negative and as the temperature is decreased, the model presents additional complications.

As a final word, it should be mentioned that the presented work only cites the works with some possible similarities, but unfortunately, none of them presents the site of a lattice occupied by a diatomic molecule; thus, possible comparisons were not able to made.

Funding Open access funding provided by the Scientific and Technological Research Council of Türkiye (TÜBİTAK).

Data Availability Statement Data sharing not applicable to this article as no datasets were generated or analyzed during the current study.

Declarations

Conflict of interest The authors declare that they have no conflict of interest.

Open Access This article is licensed under a Creative Commons Attribution 4.0 International License, which permits use, sharing, adaptation, distribution and reproduction in any medium or format, as long as you give appropriate credit to the original author(s) and the source, provide a link to the Creative Commons licence, and indicate if changes were made. The images or other third party material in this article are included in the article's Creative Commons licence, unless indicated otherwise in a credit line to the material. If material is not included in the article's Creative Commons licence and your intended use is not permitted by statutory regulation or exceeds the permitted use, you will need to obtain permission directly from the copyright holder. To view a copy of this licence, visit http://creativecommons.org/licenses/by/4.0/.

Appendix

The ERRs are given explicitly as:

$$\begin{aligned} X_1 = [&e^{\beta(2D+J_{A^0A^1}+J_{A^0B^1}+J_{B^0A^1}+J_{B^0B^1}+J_{A^1B^1})}X_1^p + e^{\beta(D+J_{A^0A^1}+J_{B^0A^1})}X_2^p \\ &+ e^{\beta(2D+J_{A^0A^1}-J_{A^0B^1}+J_{B^0A^1}-J_{B^0B^1}-J_{A^1B^1})}X_3^p \\ &+ e^{\beta(2D-J_{A^0A^1}+J_{A^0B^1}-J_{B^0A^1}+J_{B^0B^1}-J_{A^1B^1})}X_4^p \\ &+ e^{\beta(D-J_{A^0A^1}-J_{B^0A^1})}X_5^p + e^{\beta(2D-J_{A^0A^1}-J_{A^0B^1}-J_{B^0A^1}-J_{B^0B^1}+J_{A^1B^1})}X_6^p \\ &+ e^{\beta(D+J_{A^0B^1}+J_{B^0B^1})}X_7^p + e^{\beta(D-J_{A^0B^1}-J_{B^0B^1})}X_8^p + 1.0]/Z_R, \end{aligned} \tag{15}$$

$$X_2 = [e^{\beta(2D+J_{A^0A^1}+J_{A^0B^1}+J_{A^1B^1})}X_1^p + e^{\beta(D+J_{A^0A^1})}X_2^p + e^{\beta(2D+J_{A^0A^1}-J_{A^0B^1}-J_{A^1B^1})}X_3^p + e^{\beta(2D-J_{A^0A^1}+J_{A^0B^1}-J_{A^1B^1})}X_4^p + e^{\beta(D-J_{A^0A^1})}X_5^p + e^{\beta(2D-J_{A^0A^1}-J_{A^0B^1}+J_{A^1B^1})}X_6^p + e^{\beta(D+J_{A^0B^1})}X_7^p + e^{\beta(D-J_{A^0B^1})}X_8^p + 1.0]/Z_R, \quad (16)$$

$$X_3 = [e^{\beta(2D+J_{A^0A^1}+J_{A^0B^1}-J_{B^0A^1}-J_{B^0B^1}+J_{A^1B^1})}X_1^p + e^{\beta(D+J_{A^0A^1}-J_{B^0A^1})}X_2^p + e^{\beta(2D+J_{A^0A^1}-J_{A^0B^1}-J_{B^0A^1}+J_{B^0B^1}-J_{A^1B^1})}X_3^p + e^{\beta(2D-J_{A^0A^1}+J_{A^0B^1}+J_{B^0A^1}-J_{B^0B^1}-J_{A^1B^1})}X_4^p + e^{\beta(D-J_{A^0A^1}+J_{B^0A^1})}X_5^p + e^{\beta(2D-J_{A^0A^1}-J_{A^0B^1}+J_{B^0A^1}+J_{B^0B^1}+J_{A^1B^1})}X_6^p + e^{\beta(D+J_{A^0B^1}-J_{B^0B^1})}X_7^p + e^{\beta(D-J_{A^0B^1}+J_{B^0B^1})}X_8^p + 1.0]/Z_R, \quad (17)$$

$$X_4 = [e^{\beta(2D-J_{A^0A^1}-J_{A^0B^1}+J_{B^0A^1}+J_{B^0B^1}+J_{A^1B^1})}X_1^p + e^{\beta(D-J_{A^0A^1}+J_{B^0A^1})}X_2^p + e^{\beta(2D-J_{A^0A^1}+J_{A^0B^1}+J_{B^0A^1}-J_{B^0B^1}-J_{A^1B^1})}X_3^p + e^{\beta(2D+J_{A^0A^1}-J_{A^0B^1}-J_{B^0A^1}+J_{B^0B^1}-J_{A^1B^1})}X_4^p + e^{\beta(D+J_{A^0A^1}-J_{B^0A^1})}X_5^p + e^{\beta(2D+J_{A^0A^1}+J_{A^0B^1}-J_{B^0A^1}-J_{B^0B^1}+J_{A^1B^1})}X_6^p + e^{\beta(D-J_{A^0B^1}+J_{B^0B^1})}X_7^p + e^{\beta(D+J_{A^0B^1}-J_{B^0B^1})}X_8^p + 1.0]/Z_R, \quad (18)$$

$$X_5 = [e^{\beta(2D-J_{A^0A^1}-J_{A^0B^1}+J_{A^1B^1})}X_1^p + e^{\beta(D-J_{A^0A^1})}X_2^p + e^{\beta(2D-J_{A^0A^1}+J_{A^0B^1}-J_{A^1B^1})}X_3^p + e^{\beta(2D+J_{A^0A^1}-J_{A^0B^1}-J_{A^1B^1})}X_4^p + e^{\beta(D+J_{A^0A^1})}X_5^p + e^{\beta(2D+J_{A^0A^1}+J_{A^0B^1}+J_{A^1B^1})}X_6^p + e^{\beta(D-J_{A^0B^1})}X_7^p + e^{\beta(D+J_{A^0B^1})}X_8^p + 1.0]/Z_R, \quad (19)$$

$$X_6 = [e^{\beta(2D-J_{A^0A^1}-J_{A^0B^1}-J_{B^0A^1}-J_{B^0B^1}+J_{A^1B^1})}X_1^p + e^{\beta(D-J_{A^0A^1}-J_{B^0A^1})}X_2^p + e^{\beta(2D-J_{A^0A^1}+J_{A^0B^1}-J_{B^0A^1}+J_{B^0B^1}-J_{A^1B^1})}X_3^p + e^{\beta(2D+J_{A^0A^1}-J_{A^0B^1}+J_{B^0A^1}-J_{B^0B^1}-J_{A^1B^1})}X_4^p + e^{\beta(D+J_{A^0A^1}+J_{B^0A^1})}X_5^p + e^{\beta(2D+J_{A^0A^1}+J_{A^0B^1}+J_{B^0A^1}+J_{B^0B^1}+J_{A^1B^1})}X_6^p + e^{\beta(D-J_{A^0B^1}-J_{B^0B^1})}X_7^p + e^{\beta(D+J_{A^0B^1}+J_{B^0B^1})}X_8^p + 1.0]/Z_R, \quad (20)$$

$$X_7 = [e^{\beta(2D+J_{B^0A^1}+J_{B^0B^1}+J_{A^1B^1})}X_1^p + e^{\beta(D+J_{B^0A^1})}X_2^p + e^{\beta(2D+J_{B^0A^1}-J_{B^0B^1}-J_{A^1B^1})}X_3^p + e^{\beta(2D-J_{B^0A^1}+J_{B^0B^1}-J_{A^1B^1})}X_4^p + e^{\beta(D-J_{B^0A^1})}X_5^p + e^{\beta(2D-J_{B^0A^1}-J_{B^0B^1}+J_{A^1B^1})}X_6^p + e^{\beta(D+J_{B^0B^1})}X_7^p + e^{\beta(D-J_{B^0B^1})}X_8^p + 1.0]/Z_R, \quad (21)$$

$$X_8 = [e^{\beta(2D-J_{B^0A^1}-J_{B^0B^1}+J_{A^1B^1})}X_1^p + e^{\beta(D-J_{B^0A^1})}X_2^p + e^{\beta(2D-J_{B^0A^1}+J_{B^0B^1}-J_{A^1B^1})}X_3^p + e^{\beta(2D+J_{B^0A^1}-J_{B^0B^1}-J_{A^1B^1})}X_4^p + e^{\beta(D+J_{B^0A^1})}X_5^p + e^{\beta(2D+J_{B^0A^1}+J_{B^0B^1}+J_{A^1B^1})}X_6^p + e^{\beta(D-J_{B^0B^1})}X_7^p + e^{\beta(D+J_{B^0B^1})}X_8^p + 1.0]/Z_R. \quad (22)$$

References

1. E. Ising, Z. Phys. **31**, 253 (1925)
2. M. Blume, Phys. Rev. B **141**, 517 (1965)
3. H.W. Capel, Physica B **32**, 966 (1966)
4. Y. Muraoka, M. Ochiai, T. Idogaki, N. Uryu, J. Phys. A Math. Gen. **26**, 1811 (1993)
5. K. Okamoto, N. Okazaki, T. Sakai, J. Phys. Soc. Japan **70**, 636 (2001)
6. A. Koga, N. Kawakami, Physica B **329–333**, 1267 (2003)
7. M. Kaburagi, M. Kang, T. Tonegawa, K. Okunishi, J. Phys.: Condens. Matter **16**, S765–S772 (2004)
8. T. Murashima, K. Hijii, K. Nomura, T. Tonegawa, J. Phys. Soc. Japan **74**, 1544 (2005)
9. D.P. Snowman, J. Magn. Magn. Mater. **314**, 69 (2007)
10. K. Damle, T. Senthil, Phys. Rev. Lett. **97**, 067202 (2006)

11. K. Damle, Physica A **384**, 28 (2007)
12. M. Žukovič, Phys. Lett. A **376**, 3649 (2012)
13. Y. Wu, Y. Chen, Commun. Theor. Phys. **60**, 357 (2013)
14. A.S.T. Pires, Sol. State Commun. **193**, 56 (2014)
15. E. Jurčišinová, M. Jurčišin, Phys. Lett. A **379**, 933 (2015)
16. E. Jurčišinová, M. Jurčišin, J. Stat. Mech. (2016). https://doi.org/10.1088/1742-5468/2016/09/093207
17. E. Jurčišinová, M. Jurčišin, Physica A **444**, 641 (2016)
18. E. Jurčišinová, M. Jurčišin, Physica A **461**, 554 (2016)
19. B.-Z. Mi, Solid State Commun. **251**, 79 (2017)
20. A. Yogi, A.K. Bera, A. Maurya, R. Kulkarni, S.M. Yusuf, A. Hoser, A.A. Tsirlin, A. Thamizhavel, Phys. Rev. B **95**, 024401 (2017)
21. Z. El Maddahi, M.Y. El Hafidi, M. El Hafidi, Scient. Reports **9**, 12364 (2019)
22. K. Hida, J. Phys. Soc. Japan **89**, 024709 (2020)
23. K. Karľová, J. Strečka, M. Hagiwara, J. Magn. Magn. Mater. **542**, 168587 (2022)
24. N.P. Konstantinidis, Phys. Rev. B **72**, 064453 (2005)
25. S.C. Furuya, T. Giamarchi, Phys. Rev. B **89**, 205131 (2014)
26. E. Ghorbani, F. Shahbazi, Hamid Mosadeq, J. Phys.: Condens. Matter **28**, 406001 (2016)
27. R. Yu, P. Goswami, Q. Si, Phys. Rev. B **84**, 094451 (2011)
28. D. Maiti, M. Kumar, Phys. Rev. B **100**, 245118 (2019)
29. A. Nakasu, K. Totsuka, Y. Hasegawa, K. Okamoto, T. Sakai, J. Phys.: Condens. Matter **13**, 7421 (2001)
30. Y. Belmamoun, H. Ez-Zahraouy, M. Kerouad, J. Supercond. Nov. Magn. **25**, 463 (2012)
31. P.F. Dias, R.D. Niederle, P.P. Tadielo, K. Karľová, M. Schmidt, Physica E **154**, 115807 (2023)
32. S. Reja, S. Nishimoto, Phys. Rev. B **99**, 134420 (2019)
33. T. Hikihara, T. Momoi, A. Furusaki, H. Kawamura, Phys. Rev. B **81**, 224433 (2010)
34. R.F. Bishop, P.H.Y. Li, O. Götze, J. Richter, Phys. Rev. B **100**, 024401 (2019)
35. R.F. Bishop, P.H.Y. Li, Phys. Rev. B **96**, 224416 (2017)
36. T. Sakai, N. Okazaki, K. Okamoto, K. Kindo, Y. Narumi, Y. Hosokoshi, K. Kato, K. Inoue, T. Goto, Physica B **329–333**, 1203 (2003)
37. T. Sakai, N. Okazaki, K. Okamoto, K. Kindo, Y. Narumi, Y. Hosokoshi, K. Kato, K. Inoue, T. Goto, Phys. Stat. Sol. (b) **236**, 429 (2003)
38. E. Janod, C. Payen, F.-X. Lannuzel, K. Schoumacker, Phys. Rev. B **63**, 212406 (2001)
39. T. Matsushita, N. Hamaguchi, K. Shimizu, N. Wada, W. Fujita, K. Awaga, A. Yamaguchi, H. Ishimoto, J. Phys. Soc. Japan **79**, 093701 (2010)
40. Y. Shirata, H. Tanaka, T. Ono, A. Matsuo, K. Kindo, H. Nakano, J. Phys. Soc. Japan **80**, 093702 (2011)
41. T.L. Phan, D. Grinting, S.C. Yu, N.V. Dai, N.V. Khiem, J. Korean Phys. Soc. **61**, 1439 (2012)
42. E.T. Connolly, J. Phys.: Condens. Matter **30**, 025801 (2018)
43. Y.-D. Zheng, Z. Mao, B. Zhou, Chin. Phys. B **26**, 070302 (2017)
44. D. Boldrin, F. Johnson, R. Thompson, A.P. Mihai, B. Zou, J. Zemen, J. Griffiths, P. Gubeljak, K.L. Ormandy, P. Manuel, D.D. Khalyavin, B. Ouladdiaf, N. Qureshi, P. Petrov, W. Branford, L.F. Cohen, Adv. Funct. Mater. **29**, 1902502 (2019)
45. E.S. Klyushina, J. Reuther, L. Weber, A.T.M.N. Islam, J.S. Lord, B. Klemke, M. Månsson, S. Wessel, B. Lake, Phys. Rev. B **104**, 064402 (2021)
46. S. Gondh, K. Kumar, M.P. Saravanan, A.K. Pramanik, J. Phys.: Condens. Matter **35**, 48LT01 (2023)
47. P. Puphal, M. Bolte, D. Sheptyakov, A. Pustogow, K. Kliemt, M. Dressel, M. Baenitze, C. Krellner, J. Mater. Chem. C **5**, 2629 (2017)
48. E. Albayrak, M. Keskin, J. Magnet. Magnet. Mater. **261**, 196 (2003)
49. E. Albayrak, M. Keskin, E. Albayrak, Commun. Theor. Phys. **68**, 361 (2017)
50. E. Albayrak, M. Keskin, E. Albayrak, Chinese J. Phys. **56**, 622 (2018)
51. E. Albayrak, Physica A **390**, 1529 (2011)